

Acoustic attenuation compensation in photoacoustic tomography: Application to high-resolution 3D imaging of vascular networks in mice

Bradley E. Treeby^{*†}, Jan G. Laufer^{*}, Edward Z. Zhang^{*}, Francesca C. Norris[†], Mark F. Lythgoe[†], Paul C. Beard^{*} and B. T. Cox^{*}

^{*}Department of Medical Physics and Bioengineering, University College London, Gower Street, London WC1E 6BT, UK

[†]Centre for Advanced Biomedical Imaging, Department of Medicine and UCL Institute of Child Health, University College London, Gower Street, London WC1E 6BT, UK

ABSTRACT

The reconstruction algorithms commonly used in photoacoustic tomography do not account for the effects of acoustic attenuation on the measured time-domain signals. For experimental measurements made in biological tissue, acoustic attenuation causes the high frequency components of the generated ultrasound signals to be significantly reduced. When this signal loss is neglected, it manifests as a depth dependent magnitude error and blurring of features within the reconstructed photoacoustic image. Here, the approach described by Treeby *et al.* [Inverse Problems **26**(11), p. 115003, 2010] is applied to the reconstruction of high-resolution three-dimensional photoacoustic images of vascular networks around the abdomen of a pregnant female mouse. The reconstruction is based on the idea of time reversal in which a numerical model of the acoustic forward problem is run backwards in time. Compensation of acoustic attenuation in the inverse problem is achieved by using a forward model that accurately accounts for the frequency dependent attenuation experimentally observed in biological tissue. The regularisation of the inverse problem is discussed, and the methodology demonstrated through the reconstruction of several images. Clear improvements in image magnitude and resolution are seen when attenuation compensation is included.

Keywords: acoustic attenuation compensation, time reversal, image reconstruction, small animal imaging, mouse embryo, k-Wave toolbox

1. INTRODUCTION

The recent increase in popularity of photoacoustic tomography (PAT) as a preclinical imaging modality has engendered a large number of improvements in the reconstruction algorithms used to form images. Over the last decade, reconstruction algorithms have moved from ad-hoc approaches based on beam forming and inversion of the linear Radon transform to more accurate techniques based on the fast Fourier transform (FFT), inversion of the spherical Radon transform, and time reversal.¹ Particular attention has been given to compensating for the partial view problem (in which the sensor does not completely surround the object and thus does not collect all the data needed for an exact reconstruction),^{2,3} accounting for acoustic heterogeneities,^{4,5} and improving the speed of real time reconstructions.^{6,7} However, until recently, the effect of acoustic attenuation on photoacoustic images has received little attention. This is significant because over the ultrasonic frequencies relevant to photoacoustics, the acoustic attenuation in biological tissue follows a frequency power law of the form

$$\alpha = \alpha_0 \omega^y \quad (1)$$

(here α is the absorption coefficient in Nepers/m, ω is the angular frequency in rad/s, α_0 is the power law coefficient in Nepers (rad/s)^{-y} m⁻¹, and y is the power law exponent which is usually between 1 and 2). As a

[†]B.E. Treeby is now with the College of Engineering and Computer Science, The Australian National University, Canberra, ACT 0200, AUSTRALIA. Send correspondence to bradley.treeby@anu.edu.au or bencox@medphys.ucl.ac.uk. UCL photoacoustic imaging group website: <http://www.medphys.ucl.ac.uk/research/mle>

result, the high frequency components of the ultrasound waves generated in photoacoustics can be significantly diminished when they reach the detector, even if they have only travelled a short distance.⁸ Depending on the sensitivity of the detector, the properties of the incident light pulse, and the depth and characteristics of the targeted tissue chromophores (the light absorbing structures that give rise to the initial pressure distribution), the time-domain pressure signals recorded at the tissue surface may only contain a bandlimited subset of the frequencies within the original photoacoustic signal. In particular, any high frequency components that are below the measurement noise floor when they reach the transducer will not be detected. This is significant because the high frequency components are required to resolve small structures and sharp edges within the reconstructed photoacoustic image.

Previous approaches to acoustic attenuation compensation in PAT have included depth independent sharpening,⁹ thresholded matrix inversion,¹⁰ singular value decomposition,¹¹ and time reversal.^{12, 13} Several mathematical treatments of the inverse problem have also recently appeared.^{14–17} However, the application of these approaches has been limited either by computational complexity, or by the inaccuracy of the absorption model used. Recently, an alternate method for attenuation compensation was proposed based on the idea of time reversal (in which a forward model of the acoustic problem is run backwards in time) using a wave equation which accounts for tissue-realistic absorption.¹⁸ This represents an extension of an earlier idea (discussed in Ref. 12) to three-dimensions and arbitrary power law absorption. Here, this reconstruction approach is applied to high-resolution three-dimensional imaging of the vascular networks around the abdomen of a pregnant female mouse. The governing acoustic equations are described, and their application to time reversal is discussed. The experimental results are then introduced, and the improvements in image magnitude and resolution when compensation for acoustic attenuation is included are demonstrated.

2. COMPENSATION OF ACOUSTIC ATTENUATION USING TIME REVERSAL

2.1. Acoustic forward model

The acoustic forward model is based on three coupled linearised constitutive equations for media with power law absorption.¹⁹ These correspond to, respectively, an equation of motion (conservation of momentum), an equation of continuity (conservation of mass), and a lossy equation of state

$$\begin{aligned} \frac{\partial \mathbf{u}}{\partial t} &= -\frac{1}{\rho_0} \nabla p, & \frac{\partial \rho}{\partial t} &= -\rho_0 \nabla \cdot \mathbf{u}, \\ p &= c_0^2 \left\{ 1 + \tau \frac{\partial}{\partial t} (-\nabla^2)^{y/2-1} + \eta (-\nabla^2)^{(y+1)/2-1} \right\} \rho. \end{aligned} \quad (2)$$

Here, \mathbf{u} is the particle velocity, p is the acoustic pressure, ρ_0 and ρ are the ambient and acoustic densities, respectively, c_0 is the sound speed, and τ and η are proportionality coefficients given by $\tau = -2\alpha_0 c_0^{y-1}$ and $\eta = 2\alpha_0 c_0^y \tan(\pi y/2)$. The three bracketed terms in the equation of state separately account for the adiabatic, absorption, and dispersion. The absorption term is valid for $0 < y < 3$ while the dispersion term is valid for $0 < y < 3$ and $y \neq 1$. The three coupled constitutive equations can also be combined to give a second order wave equation for lossy media with power law absorption

$$\left\{ \nabla^2 - \frac{1}{c_0^2} \frac{\partial^2}{\partial t^2} + \tau \frac{\partial}{\partial t} (-\nabla^2)^{y/2} + \eta (-\nabla^2)^{(y+1)/2} \right\} p = 0. \quad (3)$$

2.2. Time reversal

In time reversal image reconstruction, the time-domain photoacoustic signals recorded at the tissue surface are applied in time-reversed order within a numerical simulation as a Dirichlet boundary condition (meaning that the pressure values are enforced; see Fig. 1). The time step in the simulation is chosen to match the sampling interval in the data acquisition, and the simulation dimensions are chosen to reflect the spatial position of the physical sensor elements and the domain of interest. At each time step, the recorded pressure values are enforced at the positions of the sensor elements within the numerical simulation. The wave field within the

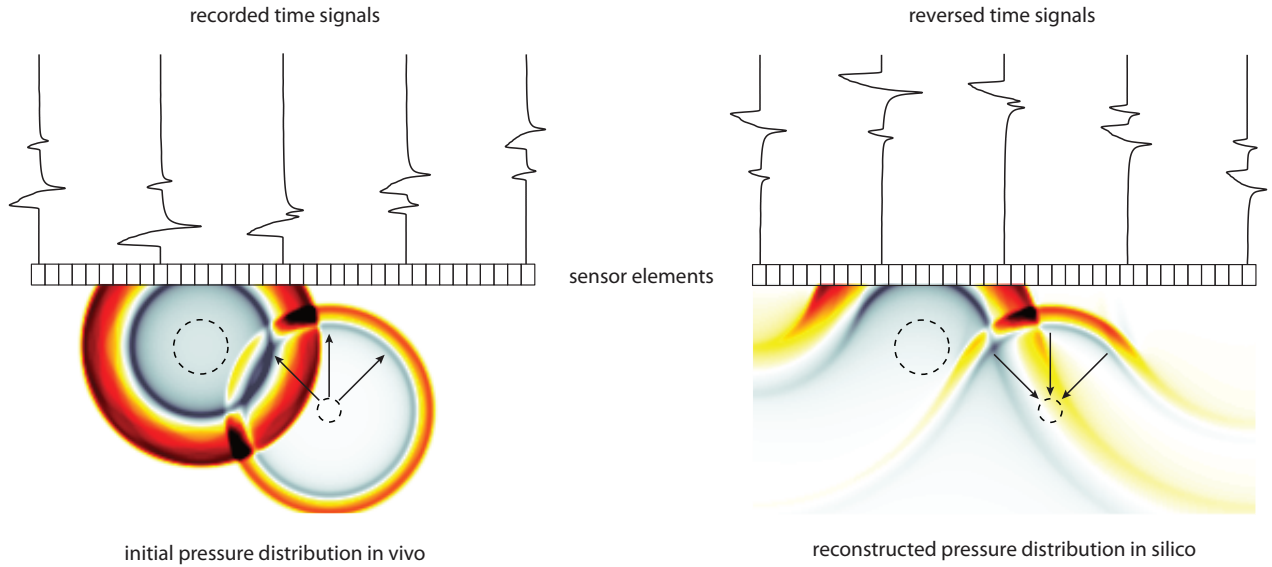


Figure 1. Photoacoustic image reconstruction using time reversal.

computational domain at the next time step is then computed using a discretised numerical version of Eq. (2). This process continues until all the recorded sensor data has been applied (i.e., the reconstruction runs for the same length of time as the recorded sensor data). It is useful to note that the general technique is applicable to any closed or open measurement geometries and can be used for both homogeneous and heterogeneous media in one, two, and three dimensions.^{5, 20–25}

When the constitutive equations given in Eq. (2) are used in forward mode, the propagating waves are absorbed according to Eq. (1). However, in time reversal image reconstruction the frequency content must instead grow according to this expression rather than decay. Consequently, the absorption proportionality coefficient τ must be reversed in sign. Conversely, the dispersion proportionality coefficient η should be left unchanged (this parameter controls the frequency dependent dispersion or dependence of the sound speed on frequency). The reason this parameter is not reversed can be explained as follows. If the high frequency components of the wave field have travelled to the detector faster than the low frequency components (as is the case for photoacoustic signals in biological tissue), they again need to travel faster than the low frequency components in the time reversal reconstruction to regain their initial position within the medium.

If a photoacoustic image is reconstructed from real or noisy data as described above, the high frequency content (where the signal to noise ratio is typically quite low) can quickly grow to mask the low frequency content, effectively obscuring the desired features within the image. This is because, as the waves propagate the high frequencies are increased at a much faster rate (recall the acoustic attenuation in soft biological tissue follows a frequency power law). To avoid this, the absorption and dispersion parameters in Eq. (2) are filtered using a frequency domain Tukey window.¹⁸ This regularises the reconstruction (in effect, stops it from ‘blowing up’) by restricting the range of frequencies that are allowed to grow. The use of a Tukey window (or tapered cosine) allows the correct frequency dependence of the absorption and dispersion within the filter passband to be maintained. An appropriate filter cutoff frequency can be selected by computing the average power spectrum of the recorded time-domain signals and finding where this spectrum reaches the noise floor.¹⁸

2.3. Computations using the k-Wave toolbox

The attenuation compensated time reversal reconstructions presented in the following sections were performed using k-Wave (a free acoustics toolbox for MATLAB available from <http://www.k-wave.org>).²⁶ This toolbox provides a fast k -space pseudo-spectral implementation of Eq. (2) including an absorbing boundary layer.^{26–28} The reconstructions were run on an NVIDIA GeForce GTX 480 graphical processing unit (GPU) using k-Wave

in conjunction with GPUmat (a free GPU toolbox for MATLAB available from <http://www.gp-you.org>). Using these tools, each three-dimensional reconstruction was completed in less than 5 minutes.

An example of using k-Wave (version B.0.3) to perform a time reversal reconstruction for a planar measurement transducer is given below. In this case, N_x and N_y correspond to the number of sensor elements in the x and y directions, dx and dy are the element spacings, N_t is the number of temporal points in the recorded sensor data, dt is the sampling interval, and `sensor_data` is a three dimensional matrix containing the recorded time signals indexed as (x, y, t) . The power law absorption properties are set using `medium.alpha_coeff` and `medium.alpha_power` which correspond to α_0 and y , respectively, where the absorption in the simulation is specified in units of dB/cm. The GPUmat toolbox is used by setting the optional input parameter 'DataCast' to 'GPUsingle'.

```
% assign the medium properties
medium.sound_speed = 1550;           % [m/s]
medium.alpha_coeff = 0.75;           % [dB/(MHz^y cm)]
medium.alpha_power = 1.5;

% reverse the sign of the absorption proportionality coefficient
medium.alpha_sign = [-1, 1];         % [absorption, dispersion]

% create a k-Wave grid structure based on the detector size and acquisition settings
kgrid = makeGrid(Nx, dx, Ny, dy, Nt, dt*medium.sound_speed);

% create the time array based on the acquisition settings
kgrid.t_array = 0:dt:(Nt - 1)*dt;   % [s]

% create a filter to regularise the absorption parameters
cutoff_freq = 25e6;                  % [Hz]
medium.alpha_filter = getAlphaFilter(kgrid, medium, cutoff_freq);

% create a binary mask of the planar sensor
sensor.mask = zeros(kgrid.Nz, kgrid.Nx, kgrid.Ny);
sensor.mask(1, :, :) = 1;

% assign the recorded sensor data to the time reversal field
sensor.time_reversal_boundary_data = squeeze(reshape(sensor_data, Nx*Ny, 1, []));

% set the input arguments for the computation
input_args = {'PMLInside', false, 'DataCast', 'GPUsingle', 'PlotSim', false};

% run the time reversal reconstruction
pa_image = kspaceFirstOrder3D(kgrid, medium, [], sensor, input_args{:});
```

3. EXPERIMENTAL RESULTS

3.1. Experimental methods

To demonstrate the applicability of the reconstruction method to experimental imaging, photoacoustic images of a sacrificed pregnant female mouse (type CD-1) with several embryos (15.5 days post coitum) were obtained using a tomography system based on a high-sensitivity planar Fabry-Perot sensor (see Fig. 2(a)).^{29–33} The mouse was illuminated in backward mode by the output of a fibre coupled optical parametric oscillator pumped by the 355 nm frequency tripled output of a Q-switched Nd:YAG laser. The pulse duration, repetition frequency, and wavelength used were 7 ns, 50 Hz, and 620 nm, respectively. The output of the beam was expanded to a diameter of approximately 2 cm at the skin surface giving an incidence fluence of less than 10 mJ cm⁻². A 16

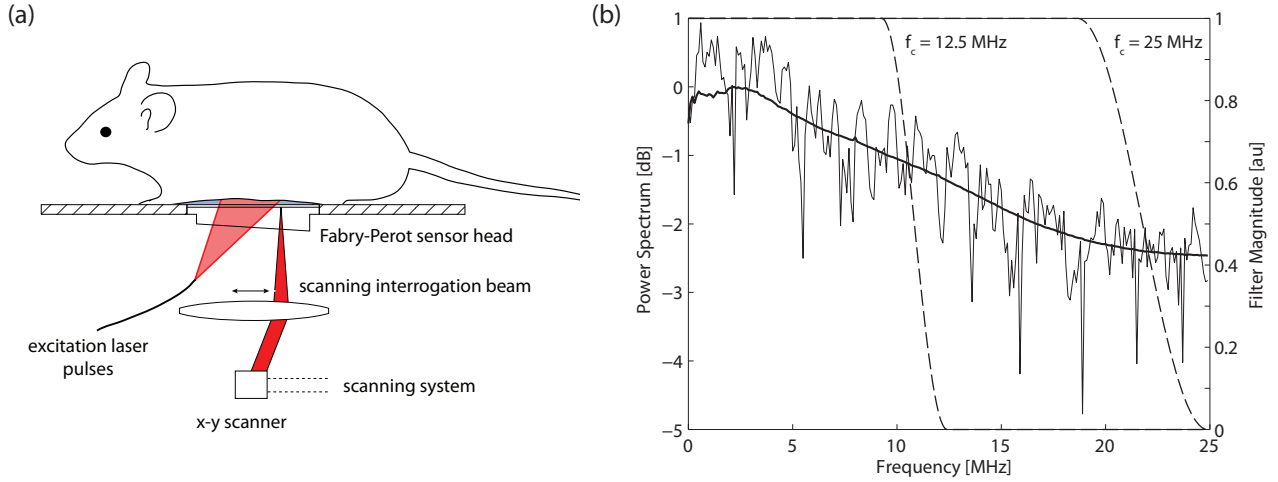


Figure 2. (a) Experimental measurement using a high-sensitivity Fabry-Perot sensor. The mouse is illuminated in backward mode using a 50 Hz Q-switched laser. The Fabry-Perot interferometer is interrogated by a second laser to acquire the photoacoustic signals. (b) Average power spectrum of the recorded time-varying pressure signals (bold line). The spectrum from the signal recorded at the central sensor element is shown for comparison (solid line). The two filters used to regularise the absorption parameters when attenuation compensation is included are also shown (dashed lines).

$\times 16$ mm area scan with a step size of $115 \mu\text{m}$ was performed, with each waveform acquired for $10 \mu\text{s}$ with a temporal resolution of 20 ns. The waveforms were acquired without signal averaging and later shortened to $5.4 \mu\text{s}$. The mouse was imaged within 1 hour of sacrifice with the complete scan taking approximately 7 minutes. The average power spectrum of the recorded time-domain signals is shown in Fig. 2(b) (bold line). The power spectrum at the central sensor element is also displayed. The acquired signals are extremely broadband, with the frequency content extending from DC to 25 MHz (the maximum frequency recorded).

The images were reconstructed using time reversal with a $141 \times 141 \times 270$ voxel grid ($16 \times 16 \times 8$ mm with a 10 voxel external perfectly matched layer) supporting frequencies up to 6.7 MHz in the lateral direction and 25 MHz in the depth direction. The disparate grid size was chosen to match the utilised data acquisition and scan parameters, and the sound speed was set to 1550 m/s. For the reconstructions with attenuation compensation, the absorption parameters were set to those of breast tissue, where $\alpha_0 = 0.75 \text{ dB}/(\text{MHz}^y \text{ cm})$ and $y = 1.5$.³⁴ Two different Tukey windows were used to regularise the absorption parameters, with cutoff frequencies of 12.5 MHz or 25 MHz in the depth direction, a cutoff frequency of 6.7 MHz in the lateral direction (equal to the maximum supported frequency), and a taper ratio of 0.25. The filter shapes are shown in Fig. 2(b). After reconstruction, the images were interpolated using Fourier interpolation to give a two-fold increase in lateral resolution. A first-order correction for the optical attenuation in tissue was also applied, where $p_{\text{corrected}} = p_{\text{reconstructed}} \times e^{\mu_{\text{eff}} z}$. Here, z corresponds to the distance in the depth direction, and a value of $\mu_{\text{eff}} = 0.15 \text{ cm}^{-1}$ was used for the effective scattering coefficient.¹⁸ The images were also reconstructed using a one-step algorithm based on the FFT for comparison.^{6, 26}

3.2. Reconstructed images

The reconstructed images are shown in Fig. 3. The plots correspond to maximum intensity projections (MIPs) through the depth and lateral dimensions and a one-dimensional profile through the lateral MIP at $y = 8.5$ mm. The superficial vasculature in the skin of the parent mouse along with the developing rib cage of the one of the embryos can be seen. When attenuation compensation is included, the edges of the superficial vessels are sharpened and the visibility of the deeper vessels is significantly improved. In particular, the magnitude of the vessel bisected by the one-dimensional profile (located at a depth of around 5.5 mm) has been discernibly enhanced, while the corresponding full width at half maximum (relative to the noise floor) has been reduced. The image reconstructed using the higher filter cutoff frequency has slightly sharper features at the expense of introducing a small amount of additional high frequency noise into the photoacoustic image. It is interesting

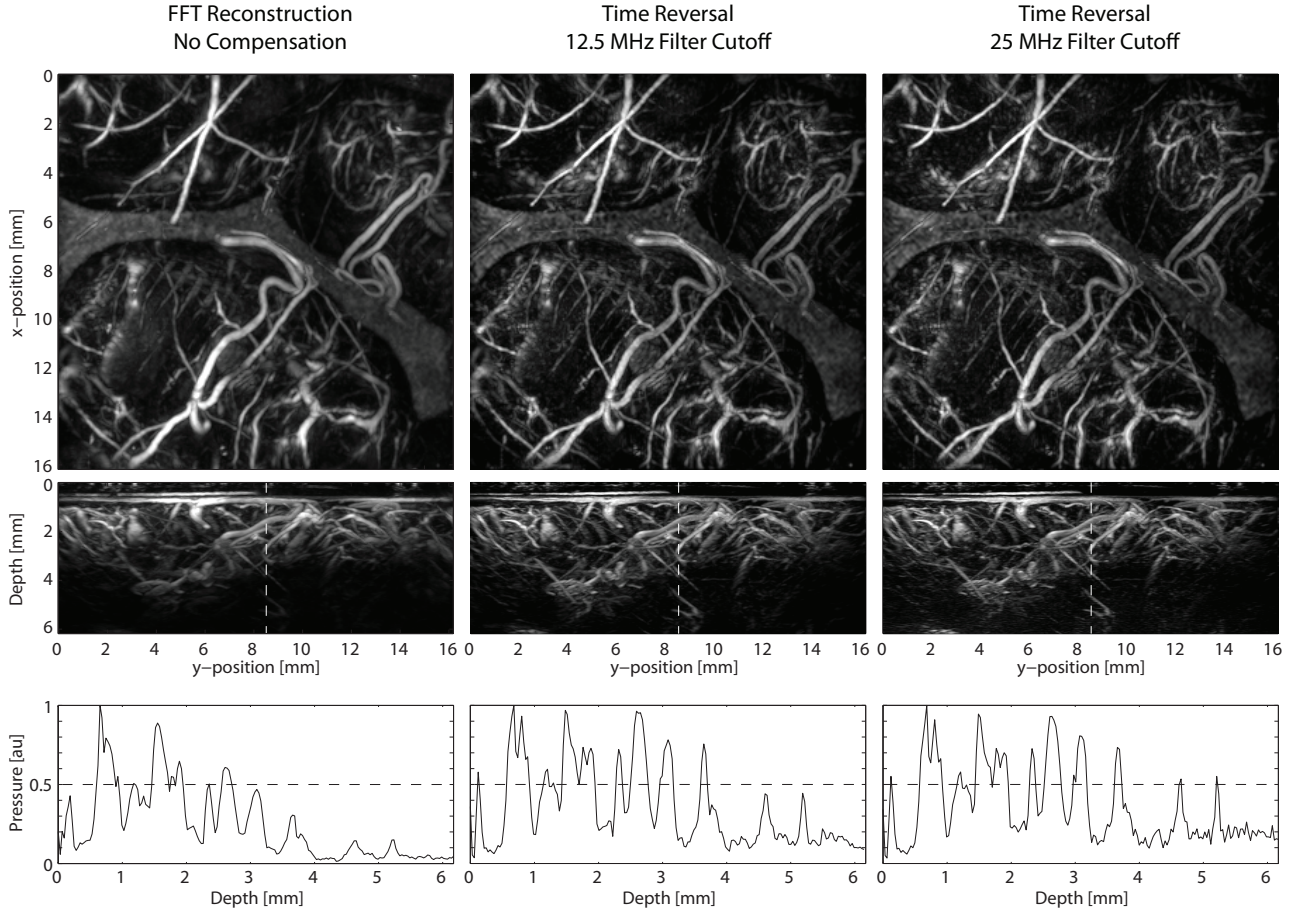


Figure 3. Three-dimensional reconstruction of the vascular networks in the abdomen of a pregnant female mouse. (a) One-step reconstruction based on the fast Fourier transform without compensation for acoustic attenuation. (b) Time reversal reconstruction including compensation for acoustic attenuation using a regularisation filter with a cutoff frequency of 12.5 MHz in the depth direction. (c) Time reversal reconstruction including compensation for acoustic attenuation using a regularisation filter with a cutoff frequency of 25 MHz in the depth direction. The three panels in each image correspond to maximum intensity projections (MIPs) through the depth and lateral directions and a one-dimensional profile through the lateral MIP at $y = 8.5$ mm (the location of the profile is shown with a dashed white line).

to note that high quality images can be obtained using time reversal even when the view angle is significantly less than 2π steradians.

Depth selective MIPs are shown in Fig. 4(a) to highlight the structures visible at different depths within the image. A labelled edge map is given in Fig. 4(b).³⁵ The superficial vasculature within the skin of the parent mouse is shown in the left panel, while the developing rib cage and cardiac systems of two embryos can clearly be seen in the central panel. The visibility of the developing bones is likely due to the increased blood supply at this stage of embryo development prior to ossification. When attenuation compensation is included, the spinal cord of the lower embryo and deeper vascular can also be clearly seen (right panel).

4. CONCLUSION

The application of attenuation compensated time reversal to image reconstruction in photoacoustic tomography has been demonstrated. Several three-dimensional reconstructions of vascular networks in the abdomen

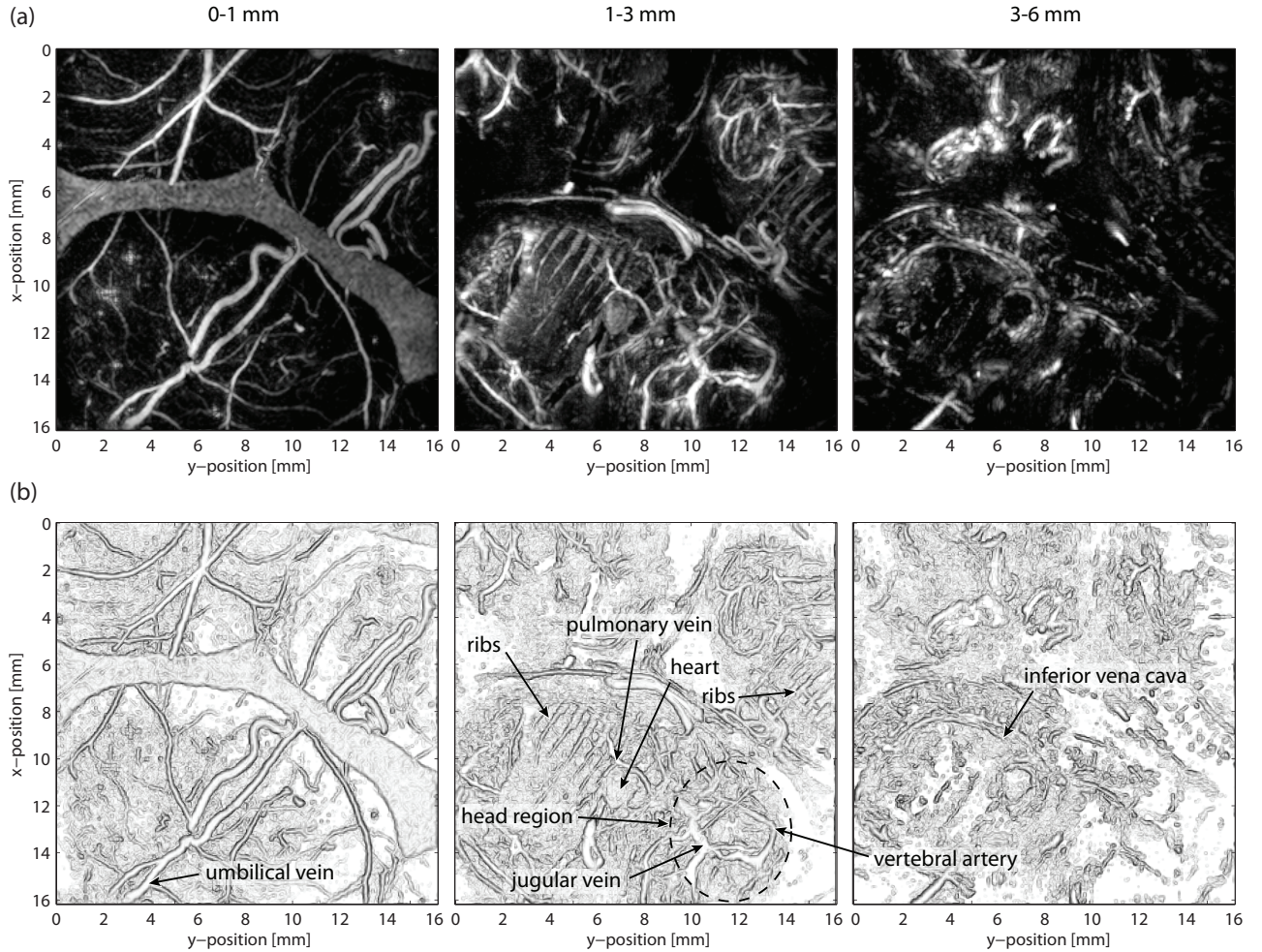


Figure 4. (a) Depth direction maximum intensity projections using sections of the reconstructed image shown in Fig. 3. The left panel corresponds to data from 0 to 1 mm, the middle panel from 1 to 3 mm, and the right panel from 3 to 6 mm. (b) Labelled edge map to illustrate features of the developing embryos within the photoacoustic image.

of a pregnant female mouse have been presented. The inclusion of attenuation compensation significantly improves the visibility of deeper features within the reconstructed images. By using a forward model based on a parallelised k -space pseudospectral method, three-dimensional reconstructions can be computed on the order of minutes, even for a dense number of sensor elements. While further work is required to characterise the required frequency dependent absorption parameters within all the biological tissues of interest, the technique provides a practical and computationally efficient way to compensate for arbitrary power law absorption in photoacoustic images derived from experimental measurements. The approach is applicable to arbitrary sensor geometries in one, two, and three dimensions, and can also be used for heterogeneous media. In addition to improving the visibility of deeper features in qualitative images, the correct reconstruction of absolute values of the initial photoacoustic pressure is also of particular importance in quantitative photoacoustic imaging.³⁶ In this case, errors in the magnitude of the reconstruction manifest as errors in the estimation of absolute chromophore concentrations.³⁷

ACKNOWLEDGMENTS

The authors would like to thank Thomas Allen for helpful discussions. This work was supported by the Engineering and Physical Sciences Research Council, UK. B.E.T. would also like to acknowledge the partial

financial support of the Australian Research Council and The Australian National University.

REFERENCES

1. P. Kuchment and L. Kunyansky, “Mathematics of thermoacoustic tomography,” *Eur. J. Appl. Math.* **19**(2), pp. 191–224, 2008.
2. Y. Xu, L. V. Wang, G. Ambartsoumian, and P. Kuchment, “Reconstructions in limited-view thermoacoustic tomography,” *Med. Phys.* **31**(4), pp. 724–733, 2004.
3. G. Paltauf, R. Nuster, and P. Burgholzer, “Weight factors for limited angle photoacoustic tomography,” *Phys. Med. Biol.* **54**, p. 3303, 2009.
4. X. Jin and L. V. Wang, “Thermoacoustic tomography with correction for acoustic speed variations,” *Phys. Med. Biol.* **51**(24), pp. 6437–6448, 2006.
5. Y. Hristova, P. Kuchment, and L. V. Nguyen, “Reconstruction and time reversal in thermoacoustic tomography in acoustically homogeneous and inhomogeneous media,” *Inverse Probl.* **24**(5), p. 055006, 2008.
6. K. P. Köstli, M. Frenz, H. Bebie, and H. P. Weber, “Temporal backward projection of optoacoustic pressure transients using Fourier transform methods,” *Phys. Med. Biol.* **46**(7), pp. 1863–1872, 2001.
7. M. Xu and L. V. Wang, “Time-domain reconstruction for thermoacoustic tomography in a spherical geometry,” *IEEE Trans. Med. Imaging* **21**(7), pp. 814–822, 2002.
8. B. E. Treeby and B. T. Cox, “Fast, tissue-realistic models of photoacoustic wave propagation for homogeneous attenuating media,” in *Proc. SPIE* **7177**, p. 717716, 2009.
9. Y. Tan, Y. W. Da Xing, and D. Yang, “Photoacoustic imaging with attenuation rectification of different frequent components of photoacoustic signal,” in *Proc. SPIE* **5630**, pp. 668–674, 2005.
10. P. J. La Rivière, J. Zhang, and M. A. Anastasio, “Image reconstruction in optoacoustic tomography for dispersive acoustic media,” *Opt. Lett.* **31**(6), pp. 781–783, 2006.
11. D. Modgil and P. J. La Rivière, “Photoacoustic image reconstruction in an attenuating medium using singular-value decomposition,” in *Nuclear Science Symposium and Medical Imaging Conference*, pp. 4489–4493, 2008.
12. P. Burgholzer, H. Grün, M. Haltmeier, R. Nuster, and G. Paltauf, “Compensation of acoustic attenuation for high-resolution photoacoustic imaging with line detectors,” in *Proc. SPIE* **6437**, p. 643724, 2007.
13. P. Burgholzer, F. Camacho-Gonzales, D. Sponseiler, G. Mayer, G. Hendorfer, “Information changes and time reversal for diffusion-related periodic fields,” in *Proc. SPIE* **7177**, p. 717723, 2009.
14. R. Kowar, “Integral equation models for thermoacoustic imaging of acoustic dissipative tissue,” *Inverse Probl.* **26**(9), p. 095005, 2010.
15. R. Kowar and O. Scherzer, “Photoacoustic imaging taking into account attenuation,” in *Proc. Mathematics and Algorithms in Tomography*, **18**, Mathematisches Forschungsinstitut Oberwolfach, 2010.
16. H. Ammari, E. Bretin, V. Jugnon, and A. Wahab, “Photoacoustic imaging for attenuating acoustic media,” in *Lecture Notes in Mathematics*, Springer-Verlag, 2011 (to be published).
17. H. Roitner and P. Burgholzer, “Efficient modeling and compensation of ultrasound attenuation losses in photoacoustic imaging,” *Inverse Probl.* **27**(1), p. 015003, 2011.
18. B. E. Treeby, E. Z. Zhang, and B. T. Cox, “Photoacoustic tomography in absorbing acoustic media using time reversal,” *Inverse Probl.* **26**(11), p. 115003, 2010.
19. B. E. Treeby and B. T. Cox, “Modeling power law absorption and dispersion for acoustic propagation using the fractional Laplacian,” *J. Acoust. Soc. Am.* **127**(5), pp. 2741–2748, 2010.
20. Y. Xu and L. V. Wang, “Application of time reversal to thermoacoustic tomography,” in *Proc. SPIE* **5320**, pp. 257–263, 2004.
21. P. Burgholzer, G. J. Matt, M. Haltmeier, and G. Paltauf, “Exact and approximative imaging methods for photoacoustic tomography using an arbitrary detection surface,” *Phys. Rev. E* **75**(4), pp. 046706–10, 2007.
22. H. Grün, R. Nuster, G. Paltauf, M. Haltmeier, and P. Burgholzer, “Photoacoustic tomography of heterogeneous media using a model-based time reversal method,” in *Proc. SPIE* **6856**, p. 685620, 2008.

23. G. Chen, Z. Zhao, Z. Nie, and Q. Liu, "Computational study of time reversal mirror technique for microwave-induced thermo-acoustic tomography," *J. Electromagn. Waves Appl.* **22**(16), pp. 2191–2204, 2008.
24. Y. Hristova, "Time reversal in thermoacoustic tomography - an error estimate," *Inverse Probl.* **25**(5), p. 055008, 2009.
25. G. Chen and Z. Zhao, "Ultrasound tomography-guide TRM technique for breast tumor detecting in MITAT system," *J. Electromagn. Waves Appl.* **11**(12), pp. 1459–1471, 2010.
26. B. E. Treeby and B. T. Cox, "k-Wave: MATLAB toolbox for the simulation and reconstruction of photoacoustic wave-fields," *J. Biomed. Opt.* **15**(2), p. 021314, 2010.
27. M. Tabei, T. D. Mast, and R. C. Waag, "A k-space method for coupled first-order acoustic propagation equations," *J. Acoust. Soc. Am.* **111**(1), pp. 53–63, 2002.
28. B. T. Cox, S. Kara, S. R. Arridge, and P. C. Beard, "k-space propagation models for acoustically heterogeneous media: Application to biomedical photoacoustics," *J. Acoust. Soc. Am.* **121**(6), pp. 3453–3464, 2007.
29. E. Z. Zhang, J. G. Laufer, and P. C. Beard, "Backward-mode multiwavelength photoacoustic scanner using a planar Fabry-Perot polymer film ultrasound sensor for high-resolution three-dimensional imaging of biological tissues," *Appl. Optics* **47**(4), pp. 561–577, 2008.
30. E. Z. Zhang, J. G. Laufer, R. B. Pedley, and P. C. Beard, "In vivo high-resolution 3D photoacoustic imaging of superficial vascular anatomy," *Phys. Med. Biol.* **54**(4), pp. 1035–1046, 2009.
31. J. Laufer, E. Zhang, G. Raivich, and P. Beard, "Three-dimensional noninvasive imaging of the vasculature in the mouse brain using a high resolution photoacoustic scanner," *Appl. Optics* **48**(10), pp. D299–D306, 2009.
32. J. G. Laufer, J. O. Cleary, E. Z. Zhang, M. F. Lythgoe, and P. C. Beard, "Photoacoustic imaging of vascular networks in transgenic mice," in *Proc. SPIE* **7564**, p. 75641A, 2010.
33. J. Laufer, J. Cleary, E. Zhang, M. Lythgoe, and P. Beard, "Photoacoustic imaging of transgenic mouse embryos," in *Biomedical Optics*, OSA Technical Digest (CD) (Optical Society of America), paper BWE7, 2010.
34. T. L. Szabo, *Diagnostic Ultrasound Imaging*, Elsevier Academic Press, London, 2004.
35. Adobe, *Photoshop CS2*, computer program, Adobe Systems Inc., San Jose, CA, 2005.
36. B. T. Cox, J. G. Laufer, and P. C. Beard, "The challenges for quantitative photoacoustic imaging," in *Proc. SPIE* **7177**, p. 717713, 2009.
37. J. Laufer, B. Cox, E. Zhang, and P. Beard, "Quantitative determination of chromophore concentrations from 2D photoacoustic images using a nonlinear model-based inversion scheme," *Appl. Optics* **49**(8), pp. 1–15, 2010.